Wall heating effects on aeroacoustic fields radiated by rigid bodies at different flow regimes

Wall heating effects on aeroacoustic fields radiated by rigid bodies at different flow regimes

Valerio D'Alessandro [a,*], Matteo Falone [a], Luca Giammichele [a], Renato Ricci [a]

[a] *Dipartimento di Ingegneria Industriale e Scienze Matematiche*
Università Politecnica delle Marche
Via Brecce Bianche 12, 60131 Ancona (AN), Italy

Abstract

This study presents several direct numerical computations concerning wall heating effects on aeroacoustic fields derived from flow-rigid body interaction. Both laminar and turbulent flow configurations involving isolated and multibody arrangements have been addressed. Some insights into the physical mechanisms concerning these problems are addressed and discussed. In particular, we observed that the aeroacoustic fields produced by laminar flows can be more easily controlled and practically suppressed in terms of acoustic emission by wall heating. By contrast, in turbulent flows, the effectiveness of the analysed technique is more limited. Indeed, wall heating produces a slight increase in overall emissions. However, at the tonal peak frequency derived from adiabatic configuration, the acoustic contribution is considerably reduced.

Key words:
Wall heating, OpenFOAM, Aeroacoustic fields, Direct Numerical Simulation

* Corresponding author.
Email address: v.dalessandro@univpm.it (Valerio D'Alessandro).

1 Introduction

Self-noise produced by aerodynamic bodies is an important issue in many applications ranging from wind turbines and helicopter rotors to fan blades and airframes, [1]. Similar problems can also be found in broad sense for bluff bodies with reference to built environment noise pollution, [2].

The flow fields derived from aforementioned application areas share unsteadiness in the boundary layer and/or in the wake region which are responsible for the creation of acoustic perturbations, [1, 3]. In this context, it is easy to understand that an aeroacoustic field can be controlled by altering the wake geometry as well as boundary layer (if present) detachment features.

Passive control techniques have been widely studied and reported. These approaches use additional objects near the reference body to mitigate acoustic disturbance, [4, 5]. Active control techniques have also received significant attention by several authors, mainly in relation to flow-field modification. Specifically, we can find some studies treating flow-field control through the imposition of line, transverse, or rotary oscillations, [6, 7]. Other techniques have even considered synthetic jets, [8]. Nevertheless, the effect of forced transverse oscillations on the sound generation and propagation from a circular cylinder immersed in uniform flow was only addressed very recently, [9, 10].

It is worth emphasising that wake geometry can also be controlled by heating the body's surface. This phenomenon was experimentally observed in a circular cylinder by Lecordier et al. [11, 12]. However, the acoustic effects related to wall heating were investigated preliminarily by D'Alessandro et al. [13], who extended their analyses to non-circular geometry sections as well. It was revealed that the wall temperature increment can reduce the aerodynamic force pulsations generated by the Karman vortex street, which is shed over bluff bodies in laminar flows. In this context, any reduction in lift pulsations is crucial because it leads to aeroacoustic perturbations decay. With the present study, we want to advance the state–of–art concerning the wall heating consequences on the aeroacoustic sound generation and propagation. In particular, the role of dynamic viscosity and flow/sound problems involving more than one body are investigated. In addition, we investigated the thermal effect on the aeroacoustic sound emitted using an NACA 0012 airfoil under turbulent flow. This is a particular aspect of the novelty of this study. In fact, at the time of writing, the impact of wall heating on aeroacoustic fields had not yet been studied in a similar flow regime.

Direct computation of the flow and acoustic fields was adopted as an analysis tool. In particular, an open-source solver called `caafoam`, developed by the authors themselves, [13], was adopted.

The remainder of this paper is organised as follows, the governing equations are presented in Section 2, while the adopted numerical discretisation techniques are briefly discussed in Section 3. Section 4 is devoted to numerical results. The conclusions are presented in Section 5 .

2 Flow model

The flow model equations, based on the conservative variables $\mathbf{u} = (\rho, \rho u_i, \rho E)^T$, are as follows:

$$\frac{\partial \mathbf{u}}{\partial t} + \boldsymbol{\nabla} \cdot \mathbf{F}_c(\mathbf{u}) - \boldsymbol{\nabla} \cdot \mathbf{F}_v(\mathbf{u}, \boldsymbol{\nabla}\mathbf{u}) = \sigma(\mathbf{u}_{ref} - \mathbf{u}), \quad (1)$$

where $\mathbf{F}_c(\mathbf{u})$ and $\mathbf{F}_v(\mathbf{u}, \boldsymbol{\nabla}\mathbf{u})$ are convective and viscous fluxes, respectively, given by:

$$\mathbf{F}_{\mathbf{c},\mathrm{j}} = \begin{pmatrix} \rho u_j \\ \rho u_1 u_j + p\delta_{1j} \\ \rho u_2 u_j + p\delta_{2j} \\ \rho u_3 u_j + p\delta_{3j} \\ \rho u_j H \end{pmatrix}, \quad \mathbf{F}_{\mathbf{v},\mathrm{j}} = \begin{pmatrix} 0 \\ \tau_{1j} \\ \tau_{2j} \\ \tau_{3j} \\ \tau_{ji} u_i - q_j \end{pmatrix}. \tag{2}$$

The viscous stress tensor is computed using the constitutive relation for Newtonian fluids, whereas for heat flux vector components, the Fourier postulate is used

$$\tau_{ij} = \mu \left(\frac{\partial u_i}{\partial x_j} + \frac{\partial u_j}{\partial x_i} - \frac{2}{3}\frac{\partial u_k}{\partial x_k}\delta_{ij} \right), \quad q_j = -\lambda \frac{\partial T}{\partial x_j}. \tag{3}$$

In this study, the dynamic viscosity μ was handled in two different ways. In the first case, a constant value was imposed, whereas the Sutherland law [14] was adopted in the second approach. However, the thermal conductivity was obtained using the Prandtl number.

The pressure was computed by assuming the ideal gas equation of state as a thermodynamic model. By contrast, the fluid temperature was evaluated employing the internal energy equation according to:

$$p = \rho(\gamma - 1)\left(E - \frac{1}{2} u_k u_k \right). \quad c_v T = E - \frac{1}{2} u_k u_k. \tag{4}$$

The last term, in the right-hand side of eq. 1 is not physical and represents the expression of the artificial sponge layer [15, 16]; this term avoids spurious wave reflections at the external boundaries, producing damping of the flow variables to a fixed reference solution, $\mathbf{u}_{ref}$.

In our approach the spatially varying coefficient σ was defined as follows:

$$\sigma = \sigma_0 \left(\frac{L_{sp} - d}{L_{sp}} \right)^n \tag{5}$$

where L_{sp} denotes the layer width, d denotes the minimum distance from the inflow/outflow boundaries, σ_0 is a constant value, and n is an integer parameter controlling the shape of the sponge profile.

The optimal sponge layer design is a complex problem, [17]. The two main parameters to consider in order to avoid sponge failure are -η_{target}, which defines the sponge strength, and the sponge width. The first one is defined as follows:

$$-\eta_{target} = 20 \frac{2 \log_{10} e}{1 - M_\infty^2} \int_{L_{sp}} \sigma d\mathbf{x}. \tag{6}$$

and it is expressed in dB. By contrast, the sponge width must be set with the following constraint for its dimensionless expression:

$$0.5 \leq \frac{L_{sp} \cdot f}{a_\infty} \leq 2 \tag{7}$$

where f is the sound disturbance frequency and a_∞ is the speed of sound, [17]. For all the laminar flow computations presented in this study, we fixed $n = 2$ in eq. 5, while the dimensionless parameter $\left(L_{sp} \cdot f\right)/a_\infty$ was 0.5 in order to limit the computational load. It is important to point out that the sponge layer dimensionless width is based on the characteristic frequency derived from the spectral analysis of the lift coefficient time-history obtained using the adiabatic wall condition. The sponge strength is provided for every configuration in their respective sections. Finally, the sponge layer size for the turbulent flow case is described in detail in Sec. 4.4.

3 Numerical approximation

The flow governing equations were solved using a collocated cell-centred finite volume method, available within the OpenFOAM v2.3.x library [18]. The code's object-oriented structure enables users to implement their own models and solvers in the baseline codes with relatively little effort (for example [19, 20, 21]), and that is why it has been receiving significant interest from the CFD community in recent years.

In particular, our solution strategy relies on a solver, called `caafoam`, developed by our research group [13], and has already proven to be reliable for direct computations of the aeroacoustic sound.

The convective part of the Eulerian flux was computed by following Pirozzoli's energy-conserving scheme [22], whereas standard central schemes for diffusive contributions were adopted. For time integration, 2N storage explicit Runge–Kutta (ERK) was employed. In particular, we considered a five-stage, fourth-order accurate ERK scheme available in the open literature [23]. In our computational experience, this scheme was appealing showed very good parallel performance and it allowed for the use of a maximum Courant number equal to 1.

4 Results

In this section we present several low Mach number cases involving uniform velocity inlet boundary condition. The cases of a single circular and two square cylinders placed side by side, as well as in a tandem configuration, were analysed. In all the aforementioned cases, the Mach number of the undisturbed flow was $\mathrm{M}_\infty = 0.2$, $\gamma = 1.4$, and the Prandtl number Pr was 0.75. The Reynolds number, based on a reference length L_{ref}, is defined in its standard form $Re = \rho_\infty u_\infty L_{ref}/\mu_\infty$.

In addition, the flow/noise problem correlated with the NACA 0012 airfoil at a chord-based Reynolds number equal to $5 \cdot 10^4$, $\mathrm{M}_\infty = 0.4$ and $\alpha = 5°$ was investigated to assess the impact of wall heating in turbulent flow regime. Undisturbed flow parameters for NACA problem are discussed in Sec. 4.4.

The acoustic field was analysed in terms of the dimensionless fluctuating pressure, defined as

$$p' = \frac{p - \overline{p}}{\rho_\infty u_{ref}^2} \tag{8}$$

where $\overline{p}$ denotes average pressure field. For comparison with literature data, $u_{ref} = a_\infty$, for laminar flow cases. By contrast, for NACA airfoil we set $u_{ref} = u_\infty$. Polar plots containing the root mean square of p' are shown to provide evidence of sound features in the far field. The dilatation rate field $\partial u_j / \partial x_j$ was also used to visualise the acoustic waves.

Aerodynamic performance were evaluated using dimensionless drag and lift coefficients given by eq. 9:

$$C_D = \frac{2D'}{\rho u_\infty^2 A_{ref}}, \quad C_L = \frac{2L'}{\rho u_\infty^2 A_{ref}}. \tag{9}$$

Standard statistics were used to analyse C_D and C_L behaviours, such as the mean drag coefficient $\overline{C_D}$, mean lift coefficient $\overline{C_L}$, root mean square of the lift coefficient $C_{L,rms}$, root mean square of the drag coefficient $C_{D,rms}$, and the oscillation amplitudes of the force coefficients ($\Delta C_D = (C_{D,max} - C_{D,min})/2$ and $\Delta C_L = (C_{L,max} - C_{L,min})/2$). The Strouhal number is defined as:

$$\mathrm{St} = \frac{f L_{ref}}{u_\infty}. \tag{10}$$

All the solutions were obtained on distributed-memory parallel machines and the computations requiring a lower load were run on a Linux cluster with 16 Intel Xeon E5-2603v3-based nodes for 192 CPU cores operating at 1.6 GHz. The code was built using Intel compilers and an MPI library version developed by Intel. Larger cases were run on the MARCONI-100 system hosted by CINECA. In the PowerPC-based system, OpenFOAM was built using GNU compilers and IBM Spectrum MPI.

4.1 Circular cylinder

The first test case considered in this study was the sound generation by the flow past a circular cylinder at $\mathrm{Re} = 150$ where the cylinder diameter D is the reference length. We used a fully-structured O-type grid with far-field boundaries placed at 150 times D, and the height of the first cell next to the wall y_c was set to $y_c/D = 5 \cdot 10^{-3}$. To discretise the radial direction, we used 750 cells, whereas 700 were used in the azimuthal direction. Thus, the total number of cells N_c was $5.25 \cdot 10^5$. It is also important to note that this grid was already benchmarked by the authors for this kind of flow/sound field, [13]. The sponge's strength was set at 40 dB.

Two different settings were considered to investigate the effects of the thermal boundary conditions at the wall on the acoustic field, fixed wall temperatures ($T_w = 2T_\infty$ and $T_w = 3T_\infty$) and a fixed wall temperature gradient ($\partial T/\partial n|_w = 0.5$, $\partial T/\partial n|_w = 1$ and $\partial T/\partial n|_w = 2$). A baseline configuration involving an adiabatic wall was also computed.

Fig. 1 shows the directivity plot based on p'_{rms} evaluated on a circle having a radius $r/D = 75$. The effectiveness of the proposed grid and solver was demonstrated by comparing our predictions with the DNS data published by Inoue and Hakateyama, [3]. A key element is the clear dominance of lift fluctuations which yield a typical dipolar acoustic field. Fig. 2 shows p'_{rms} polar plot on a circle having a radius $r = 40\ D$ for different fixed wall temperatures. Note that we selected $r = 40\ D$ because we wanted to prevent excessive sound wave decay in the far field in order to estimate wall thermal effects on the acoustic field. The impact of the thermophysical model on dynamic viscosity was also assessed; the data reported in Fig. 2, labelled with $\mu\,(T)$ are related to the Sutherland viscosity model results, whereas the other data refer to the temperature-independent viscosity. Note that the dimensionless Sutherland constant is $S/T_\infty = 0.3855$. It is worth noting that the considered flow/sound problems, which relied on adiabatic wall conditions, experienced very limited magnitude of the temperature field gradient. This effect was the result of the wall pressure gradient distribution. Therefore, it is very clear that thermal dependent viscosity produces negligible effects when adiabatic wall boundary conditions are adopted. For non-adiabatic cases, the effect is the opposite. Tab. 1 and Tab. 2 show that non-adiabatic wall conditions produce contrasting effects on the $\overline{C_D}$. Conversely, the force coefficient pulsations and St are reduced as a result of the wall heating. It should be noted that similar results agree with those of Lecordier et al. [11, 12], who experimentally observed vortex shedding damping behind a heated circular cylinder. Moreover, vortex shedding damping, related to wall heating was confirmed for both thermo-physical models used in this study. This is extremely important to explain why far-field sound abatement occurs at higher wall temperatures. Indeed, the acoustic field derived from the fluid–body interaction is related to the sound sources damping, *i.e.* ΔC_D and ΔC_L. Furthermore, it is evident that the adoption of the Sutherland model amplified sound abatement. In fact, with the temperature-independent viscosity model, we can only account for the modification of the pressure owing to the thermal effect, that is, $p \propto T$. By contrast, when the Sutherland model was enabled, the viscosity increased with temperature; thus, we obtained $\tau_w \propto T$ (where τ_w denotes wall shear stress). Consequently, in the latter case, we increased both the wall shear stresses and the pressure gradient magnitude acting on the wall temperature. When a fixed viscosity was used, only the pressure gradient magnitude was affected by the temperature field. Owing to the previous reasons we believe that the Sutherland model-based predictions produced more significant dissipation on the flow properties in the wall region, as well as in the near-wall region. Hence, the final effect was the diminishing force oscillations with a consequent stronger p'_{rms} average value abatement.

Fig. 3 shows acoustic pressure polar plots obtained using fixed wall temperature gradient on the cylinder surface. Clearly, it can be observed that p'_{rms} exhibits a behaviour similar to that of the fixed temperature case. Nevertheless, the impact of the thermophysical model assumes even greater importance given by the magnitude of the wall temperature gradient.

Therefore, in the following, because of the augmentations reported above, we used the Sutherland model which is more physical than other models. Simultaneously, fixed-gradient boundary conditions for the temperature field were employed because they were simpler to reproduce experimentally (through Joule heating) for the sake of benchmarking.

4.1.1 Effect of local wall heating

In order to improve the understanding of the aerodynamic sound active thermal control we analysed the flow/sound fields performing localised wall heating. In other words, we generated three different configurations, namely C1, C2, and C3, and thereafter applied the wall temperature gradient to the upper and lower sides of the cylinder. The aforementioned cases differed from the angular sector extension where the conditions were imposed. In the C1 configuration, we assessed two different cases. First, we applied $\partial T/\partial n|_w > 0$ for $0° \leq \theta \leq 90°$, whereas $\partial T/\partial n|_w = 0$ for $90° < \theta \leq 180°$. In the latter, we used $\partial T/\partial n|_w = 0$ for $0° \leq \theta \leq 90°$, whereas $\partial T/\partial n|_w > 0$ for $90° < \theta \leq 180°$. Note that θ is clockwise positive and equal to $0°$ at the cylinder's leading edge (LE), whereas is $180°$ at the trailing edge (TE). On the bottom side, the boundary conditions for the temperature were symmetric with respect to the upper one. For case C2, we divided both cylinder sides into three equal parts with an angular extension $\Delta\theta = 60°$, to obtain three angular sector couples. Successively, we did not apply a null temperature gradient to each of the three couples, and the remaining part of the surface of the cylinder was adiabatic. Finally, for C3, we defined the wall boundary conditions similar to C2 with $\Delta\theta = 30°$; hence, we obtained six different cases to study. The results related to the aforementioned configurations, are showed in Fig. 4 – 6. To better estimate the acoustic damping provided by local wall heating, all polar plots also contained p'_{rms} for the fully adiabatic and heated cases, respectively, $\partial T/\partial n|_w = 0$ and $\partial T/\partial n|_w = 1$.

Looking at Fig. 4, it is interesting to note that the application of the heat flux corresponding to $\partial T/\partial n|_w = 1$ only for the cylinder forepart, $0° \leq \theta \leq 90°$, had negligible effects on the sound field. In fact, this configuration produced very similar results to a fully adiabatic condition. By contrast, $\partial T/\partial n|_w = 1$ for $90° < \theta \leq 180°$ was equivalent to the temperature gradient application on the full surface. Further shrinkage in the thermal flux application produced in the C2 case, provided evidence that almost the entire sound reduction effect can be assigned to the $120° < \theta \leq 180°$ zone, as depicted in Fig. 5. The adoption of an angular step equal to 30° improved our understanding of the discussed phenomenon. Indeed, from Fig. 6, it is clear in the two zones: $120° < \theta \leq 150°$ and $150° < \theta \leq 180°$ both contribute to sound emission reduction. However, the latter one has grater weight than the former in the overall context.

Therefore, it can be stated that wall heating focused on separated flow region is the key aspect for adequately controlling force oscillations and related sound emission.

4.2 Square cylinders arranged side by side

The subject of this subsection is sound generation around two square cylinders placed side by side, as shown in Fig. 7. L is the spacing between the centres of the two cylinders and D is their diameter. In this study, the ratio L/D was set to 3, while the Reynolds number, based on the cylinders' diameter, is 150.

This flow configuration generates a bifurcation of the wake patterns with different acoustic responses, [24]. In the following, we refer to a flow field called in literature as in-phase because it exhibits synchronised lift coefficients. It is obtained using a initial field consisting of a clockwise vortex placed behind both the upper and the lower cylinder, [24]. A fully-structured orthogonal computational grid was used, which adopted a sponge layer with a strength of 45 dB. This grid was already successfully tested for similar problems, [13]. The far field was placed 200 D from the midpoint of the two cylinders (see Fig. 7), grid cells were clustered near the cylinder wall with a dimensionless first-cell height of 10^{-2}. The number of cells had a total number of $4.44 \cdot 10^{6}$. The typical run was performed on MARCONI–100 HPC system using 192 CPU cores.

Fig. 8(a) shows a directivity plot evaluated on a circle having dimensionless radius $r/D = 75$. Overall, the results showed good agreement with the findings of Inoue et al. [24]. Thus, the usefulness of both the grid and solver was proven.

Fig. 8(b) shows acoustic pressure polar plots obtained with varying wall temperature gradient on the cylinders' surface. It can be clearly observed that in this case, the sound emission was significantly reduced owing to thermal wall flux application. Furthermore, this evidence was in good agreement with force coefficient modifications which are highlighted in Tab. 3.

4.3 Square cylinders in tandem

With the same aim as for the side-by-side arrangement, we also considered the flow and sound generation around two square cylinders in a tandem configuration at Re = 150 with $L/D = 2$, where L and D have the meaning expressed in Fig. 9.

Also in this case we have used a square computational domain with a far field placed at 200 D from the origin. Quadrilateral orthogonal cells were used to discretize the flow domain. The total number of cells, N_c, was about $4.2 \cdot 10^6$, and a grid refinement was performed near the walls of the cylinders adopting $y_c/D = 10^{-2}$ as in our previous work [13]. Acoustic wave reflections at the far boundaries were removed using a configuration derived from the previous test cases; the sponge layer's strength was 45 dB. The typical run was performed on MARCONI–100 HPC system using 192 CPU–core.

Once again, `caafoam` solver, as well as the selected grid, are in very good agreement with DNS data of Inoue [25], as showed in Fig. 10(a). In Fig. 10(b) can be noted that acoustic pressure is significantly reduced by wall heating also in this configuration. This element is corroborated by force coefficients modifications reported in Tab. 4.

It is very clear that this specific configuration put in evidence a noticeable abatement of the emitted sound if compared with the other ones previously described. In the authors' opinion this result is connected to the aerodynamic coefficients fluctuations magnitude which is the lowest for the present arrangement. Thus, the effect of the wall thermal flux is more marked than in the other flow/sound problems addressed in this work.

4.4 Turbulent flow past NACA 0012 at $\mathrm{Re} = 5 \cdot 10^4$*,* $\mathrm{M}_\infty = 0.4$ *and* $\alpha = 5^\circ$

In this subsection, the numerical results of turbulent flow past NACA 0012 are presented and discussed. Owing to the strong spanwise coherence of the pressure fluctuation for turbulent flows over airfoils operating at moderate Reynolds numbers [26], the aeroacoustic field was examined through 2-D DNS, [26, 27]. In the following, the undisturbed flow parameters were set for validation, with reference to Sandberg et al. [26] and Jones et al. [28]. In particular, we adopted the specific heat ratio, Prandtl number, and dimensionless Sutherland's constant as $\gamma = 1.4$, $\mathrm{Pr} = 0.72$, and $\mathrm{S}/\mathrm{T}_\infty = 0.3686$, respectively.

The adiabatic wall condition was fixed on the airfoil surface.

The computational domain is a C-type region that extended 7.3 times the airfoil chord length c in the radial direction and 5 c in the wake region. Four fully-structured computational grids were used to achieve grid independence in terms of both aerodynamic coefficients and acoustic pressure. All the aforementioned grids had a dimensionless height for the first cell next to the wall, y_p/c , equal to 10^{-4}. Considering the complexity of the involved phenomena, it was evident that the correct definition of the grid resolution requirements was mandatory. In this study, an iterative grid generation method was adopted to achieve a suitable mesh configuration. Cell distribution details are listed in Tab. 5. Moreover, the following numerical computations were run on the MARCONI-100 system using 192 CPU cores for the coarsest grid, whereas the finest grid typical run employed 320 CPU cores.

As briefly introduced above, the configuration considered in this study produced a complex variety of fluid phenomena. In particular, a long laminar separation bubble (LSB) with an approximate extension of 0.5 c was present on the suction side. Moreover, LSB reattachment led to vortex shedding that evolved until the TE, where the airfoil-vortices interaction generated a dipolar tonal noise. The vortical structures that convected on the suction side are shown in Fig. 11(a), whereas Fig. 11(b) provides a view of the acoustic waves through the dilatation rate field $\partial u_j/\partial x_j$. In addition, it can be clearly observed that the main acoustic source was located immediately after the airfoil TE. Table 6 provides evidence that for the coarsest grid, G1, the time-averaged lift coefficient, $\overline{C_L}$, is underestimated; however, the time-averaged drag coefficient, $\overline{C_D}$, is slightly overestimated compared with the literature data. The aerodynamic coefficients converged to those in the literature when finer grids were adopted, particularly in terms of $\overline{C_L}$. Globally, a good agreement with Jones [28] was reached for G3 and G4.

The local aerodynamic performance was estimated using the pressure coefficient $c_p = 2\left(p - p_\infty\right)/\rho_\infty u_\infty^2$, and skin friction coefficient, $c_f = 2\tau_w/\rho_\infty u_\infty^2$. In

Fig. 12(a) the mean pressure coefficient, $\overline{c_p}$, distribution is represented. It is confirmed that the G3 grid results provide an appropriate description of the flow around the NACA 0012 airfoil. In particular, the wide extension of the LSB was noticeable when looking at the plateau on the suction side, whereas $\overline{c_p}$ on the pressure side suggested that for the considered angle of attack, the airfoil lower surface had a flat plate-like behaviour.

On the contrary, Fig. 12(b) shows the mean skin friction coefficient, $\overline{c_f}$ distribution, along the airfoil chord. In this framework, it is interesting to note that as the grid resolution increased, the reattachment point moved toward the LE and the secondary separation region was better described.

In order to isolate the vortex shedding characteristic frequency and its related sound emission, a sampling probe was used to collect the pressure data. It was placed at $x/c = 0.5$ and $y/c = 0.6$. Note that the origin of the reference frame was placed on the airfoil LE, and the x-axis was aligned with the airfoil chord, as in Sandberg et al. [26]. Pressure data were sampled over a dimensionless time fixed at 120 and Fourier transformed. As shown in Fig. 13(a), a tonal peak was observed corresponding to a reduced frequency $\mu_0 = \pi f c/a_\infty (1 - \mathrm{M}_\infty^2)$, equal to 5.036. This holds true for all the considered grids.

It is worth emphasising that a critical point of this numerical computation is correlated with proper sponge layer calibration. This flow problem was performed based on the lowest significant tonal peak exhibited by the spectrum reported in Fig. 13(a). This frequency was selected to obtain $L_{sp} \cdot f/a_\infty = 1$, which implies a thicker sponge layer than in laminar configuration. A similar condition is strictly required to dissipate the vortical flow structures shed by airfoil [17]. As $L_{sp} \cdot f/a_\infty \geq 2$ can produce sponge-layer auto-reflection issues, we decided to use a compromise value to avoid an excessive overcoming of the sponge thickness upper bound. The efficacy of the previous choice coupled with $-\eta_{target} = 40$ dB is evident from Fig. 11(b), where unphysical pressure waves are not present.

The aeroacoustic noise produced in this configuration was also investigated using the polar distribution of acoustic pressure in the mean field. In this specific case, the pressure-time history was sampled over 360 equispaced probes placed along a circumference that originated from the TE and had a radius of 2 c. Fig. 13(b) highlights the dipolar nature of the acoustic field, related to the lift pulsation dominance. Moreover, it is evident that G1 did not adequately predict the airfoil sound emission, whereas G3 and G4 produced almost indistinguishable results. Furthermore, the comparison of our finest grid data with the reference ones showed slight differences; in our opinion, this was because of the peculiar LE treatment adopted by Sandberg et al. [26].

In this subsection, we provide an additional insight into the alteration of the aeroacoustic field owing to airfoil suction-side heating. Specifically, we intended to investigate whether the wall-heating effect, noted in laminar flows, was still effective in the turbulent regime. Two different configurations of wall thermal flux were analysed. In the first configuration, the dimensionless wall temperature gradient was fixed at 1, whereas in the second, we adopted $\partial T/\partial n|_w = 5$. In Fig. 14(a), we show the acoustic pressure polar plot for $\mu_0 = 5.036$, derived from adiabatic computations. It can be clearly observed that the sound emission was effectively reduced for both the wall thermal fluxes. Moreover, the tonal peak frequency moved forward to higher values, as listed in Tab. 7. Looking at Fig. 14(b) and Fig. 14(c) it is possible to observe p'_{rms} polar plots connected to the μ_0 tonal peak derived from the two thermal fluxes considered herein. It can be clearly observed that in these cases, only the configuration producing the μ_0 tonal peak had a significant impact on the sound emission. Nevertheless, the effect on the overall frequencies produced a slight p'_{rms} increase, as shown in Fig. 14(d). This is because of an opposing evidence with respect to what was observed for laminar flows. Indeed, for the turbulent configuration studied herein, the wall heating produced little amplification in the aerodynamic force pulsation (approximately 2% for $\partial T/\partial n|_w = 5$), as shown in Tab. 7. Therefore, we can conclude that the active thermal control of the aeroacoustic field derived from turbulent flows is not as effective as that in the laminar regime, in terms of acoustic power level reduction. In particular, the wall thermal flux acts as a tonal peak frequency shifter.

5 Conclusions

In this study, we investigated the effectiveness of wall heating as an active control technique for the aerodynamically generated sound and/or noise for laminar and turbulent cases. In laminar flows, we investigated both single and multiple body arrangements with reference to well established literature data. By contrast, turbulent flow analyses are limited to NACA 0012 airfoil owing to their high computational resource requirements.

Specifically, we observed that far-field sound abatement at higher wall temperatures was produced for laminar flows over bluff bodies. This is related to the reduction in aerodynamic force pulsations generated by the Karman vortex street, which is shed over bluff bodies in laminar flows. It is worth noting that a similar effect was obtained in several configurations involving more than one single body. For an isolated circular cylinder, we observed that localised wall heating produced the same effect for the overall wall heating. Moreover, thermal fluxes focused on separated flow regions is the key aspect for adequately controlling force oscillations and related sound emission.

In this study, we also addressed for the first time, the impact of wall heating on aeroacoustic field derived from a turbulent flow regime. Thus, we computed the flow and acoustic field developed around the NACA 0012 airfoil. First, we further validated our solver for turbulent flows against well-established literature benchmarks. Therefore, we observed that the sound emission was effectively lower for a reduced frequency with the same maximum tonal contribution obtained from adiabatic wall condition. However, the overall frequency contribution produced a slight p'_{rms} increase. Based on these results, we conclude that the thermal control of the aeroacoustic field derived from turbulent flows is not as effective as that in the laminar regime in terms of the acoustic power level. By contrast, the wall thermal fluxes can be considered effective as tonal peak frequency shifters. Therefore, the above discussed technique is promising for specific applications.

6 Acknowledgements

We acknowledge the CINECA Award N. HP10B3UA3N YEAR 2019 under the ISCRA initiative, for the availability of high performance computing resources and support. We acknowledge Prof. Richard Sandberg for providing us NACA 0012 data and for several useful comments on the NACA 0012 airfoil results.

References

[1] Sandberg, R.D. and Jones, L.E. Direct numerical simulations of airfoil self-noise. *Procedia Engineering*, 6:274–282, 2010. IUTAM Symposium on Computational Aero-Acoustics for Aircraft Noise Prediction.

[2] Lam, B. and Gan, W.S. and Shi, D. and Nishimura, M. and Elliott, S. Ten questions concerning active noise control in the built environment. *Building and Environment*, 200:107928, 2021.

[3] Inoue, O. and Hatakeyama, N. Sound generation by a two–dimensional circular cylinder in a uniform flow. *Journal of Fluid Mechanics*, 471:285–314, 2002.

[4] Mahato, B. and Ganta, N. and Bhumkar, Y.G. Control of aeroacoustic noise generation during flow past a circular cylinder using splitter plate. In *INTER-NOISE 2019 MADRID - 48th International Congress and Exhibition on Noise Control Engineering*, 2019.

[5] Chauhan, M.K. and Dutta, S. and Gandhi, B.K. Wake flow modification behind a square cylinder using control rods. *Journal of Wind Engineering and Industrial Aerodynamics*, 184:342–361, 2019.

[6] Bearman, P W. Vortex Shedding from Oscillating Bluff Bodies. *Ann. Rev. Fluid Mech.*, 16(1):195–222, 1984.

[7] Williamson, C.H.K. and Govardhan, R. Vortex–induced vibration. *Ann. Rev. Fluid Mech.*, 36(1):413–455, 2004.

[8] Feng, L.H. and Wang, J.J. Modification of a circular cylinder wake with synthetic jet: Vortex shedding modes and mechanism. *European Journal of Mechanics - B/Fluids*, 43:14–32, 2014.

[9] Ma, R. and Liu, Z. and Zhang, G. and Doolan, C.J. and Moreau, D.J. Control of Aeolian tones from a circular cylinder using forced oscillation. *Aerospace Science and Technology*, 94:105370, 2019.

[10] Ganta, N. and Mahato, B. and Bhumkar, Y.G. Analysis of sound generation by flow past a circular cylinder performing rotary oscillations using direct simulation approach. *Physics of Fluids*, 31(2), 2019.

[11] Lecordier, J.C. and Hamma, L. and Paranthoen, P. The control of vortex shedding behind heated circular cylinders at low Reynolds numbers. *Experiments in Fluids*, 10(4):224–229, 1991.

[12] Lecordier, J.-C. and Browne, L.W.B. and Le Masson, S. and Dumouchel, F. and Paranthoen, P. Control of vortex shedding by thermal effect at low Reynolds numbers. *Experimental Thermal and Fluid Science*, 21(4):227–237, 2000.

[13] D'Alessandro, V. and Falone, M. and Ricci, R. Direct computation of aeroacoustic fields in laminar flows: Solver development and assessment of wall temperature effects on radiated sound around bluff bodies. *Computers & Fluids*, 203:104517, 2020.

[14] Sutherland, W. . The viscosity of gases and molecular force. *The London, Edinburgh, and Dublin Philosophical Magazine and Journal of Science*, 36(223):507–531, 1893.

[15] Moshe Israeli and Steven A. Orszag. Approximation of radiation boundary conditions. *Journal of Computational Physics*, 41(1):115–135, 1981.

[16] Jesper Larsen and Henry Dancy. Open boundaries in short wave simulations – A new approach. *Coastal Engineering*, 7(3):285–297, 1983.

[17] Mani, A. Analysis and optimization of numerical sponge layers as a nonreflective boundary treatment. *Journal of Computational Physics*, 231(2):704–716, 2012.

[18] Weller, H.G. and Tabor, G. and Jasak, H. and Fureby, C. A tensorial approach to computational continuum mechanics using object–oriented techniques. *Computational Physics*, 12(6):620–631, 1998.

[19] Pham, T.Q.D. and Choi, S. Numerical analysis of direct contact condensation-induced water hammering effect using OpenFOAM in realistic steam pipes. *International Journal of Heat and Mass Transfer*, 171:121099, 2021.

[20] Barbosa, D.V.E and Santos, A.L.G. and dos Santos, E.D. and Souza, J.A. Overtopping device numerical study: Openfoam solution verification and evaluation of curved ramps performances. *International Journal of Heat and Mass Transfer*, 131:411–423, 2019.

[21] Lee, G.L. and Law, M.C. and Lee, V.C.C. Numerical modelling of liquid heating and boiling phenomena under microwave irradiation using OpenFOAM. *International Journal of Heat and Mass Transfer*, 148:119096, 2020.

[22] Pirozzoli, S. Numerical methods for high-speed flows. *Annual Review of Fluid Mechanics*, 43:163–194, 2011.

[23] Kennedy, C.A. and Carpenter, M.H. and Lewis, R.M. Low–storage, explicit Runge–Kutta schemes for the compressible Navier–Stokes equations. *Applied Numerical Mathematics*, 35(3):177 – 219, 2000.

[24] Inoue, O. and Iwakami, W. and Hatakeyama, N. . Aeolian tones radiated from flow past two square cylinders in a side-by-side arrangement. *Physics of Fluids*, 18(4):046104, 2006.

[25] Inoue, O. and Mori, M. and Hatakeyama, N. . Aeolian tones radiated from flow past two square cylinders in tandem. *Physics of Fluids*, 18(4):046101, 2006.

[26] Sandberg, R.D. and Jones, L.E. and Sandham, N.D. and Joseph, P.F. Direct numerical simulations of tonal noise generated by laminar flow past airfoils. *J. of Sound Vib.*, 320(4):838–58, 2009.

[27] Ricciardi, T.R. and Arias-Ramirez, W. and Wolf, W.R. On secondary tones arising in trailing-edge noise at moderate Reynolds numbers. *European Journal of Mechanics - B/Fluids*, 79:54–66, 2020.

[28] Jones, L. E. and Sandberg, R. D. and Sandham, N. D. Direct numerical simulations of forced and unforced separation bubbles on an airfoil at incidence. *J. Fluid Mech.*, 602:175–207, 2008.

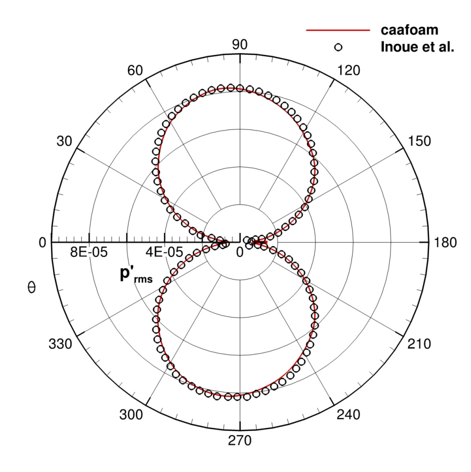

Figure 1. Flow past a circular cylinder. Solver validation.

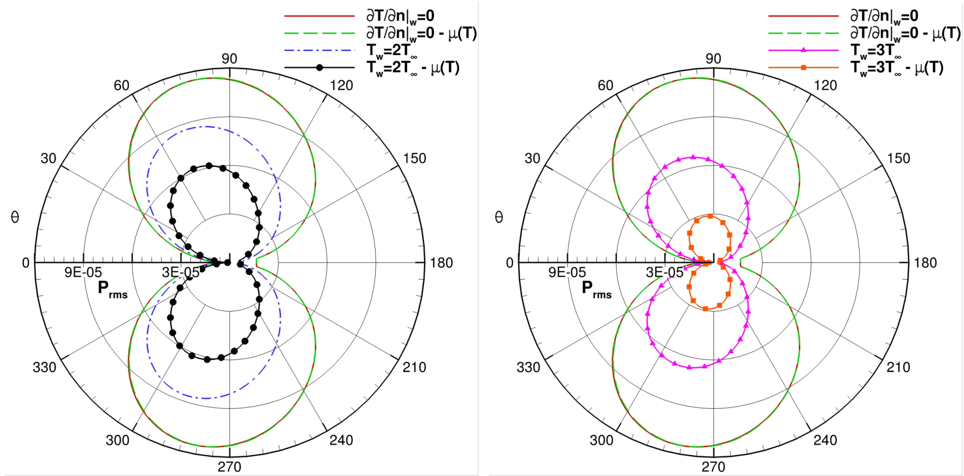

(a) $T_w = 2$ (b) $T_w = 3$

Figure 2. Flow past a circular cylinder. Fixed wall temperature effect, $r/D = 40$.

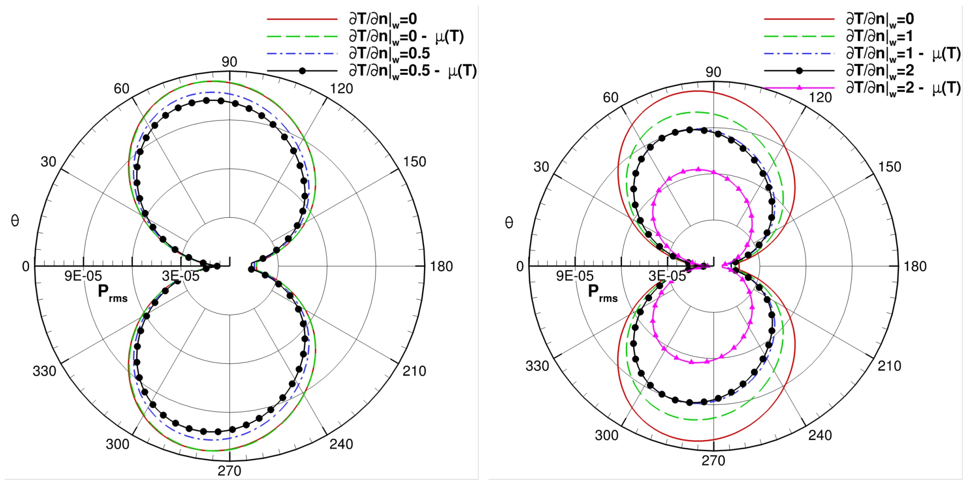

(a) $\partial T/\partial n|_w = 0$ and 0.5

(b) $\partial T/\partial n|_w = 0$, 1 and 2

Figure 3. Flow past a circular cylinder. Fixed wall temperature gradient effect, $r/D = 40$.

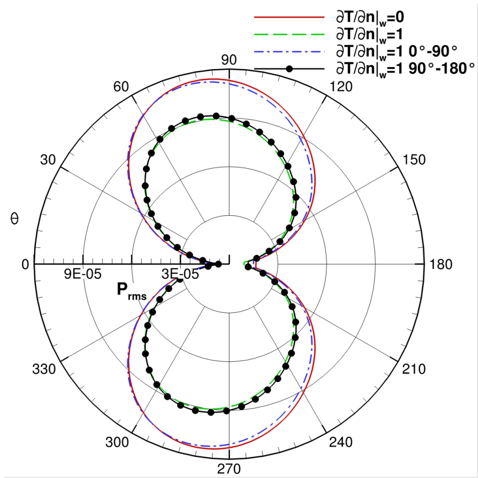

Figure 4. Flow past a circular cylinder. C1 case, $r/D = 40$.

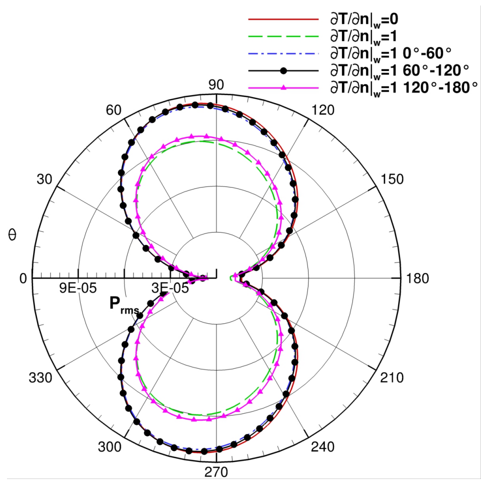

Figure 5. Flow past a circular cylinder. C2 case, $r/D = 40$.

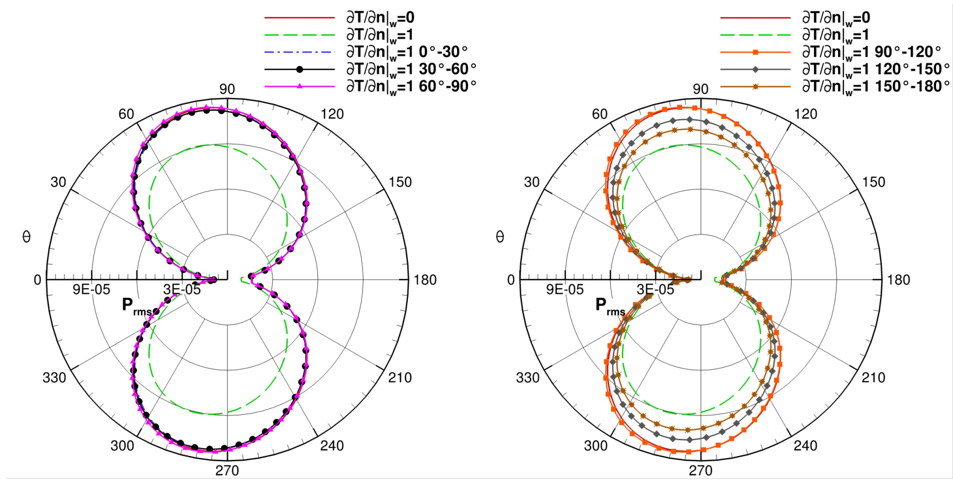

(a) $0° \leq \theta \leq 90°$ (b) $90° \leq \theta \leq 180°$

Figure 6. Flow past a circular cylinder. C3 case, $r/D = 40$.

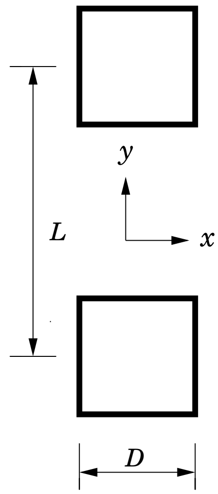

Figure 7. Cylinders arranged side by side.

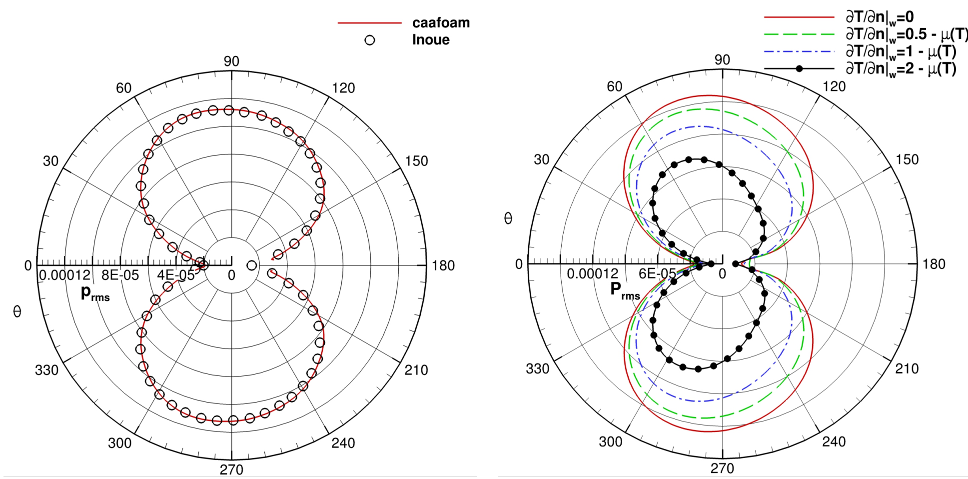

(a) Solver validation (b) Wall heating effect

Figure 8. Cylinders arranged side by side. Acoustic pressure results.

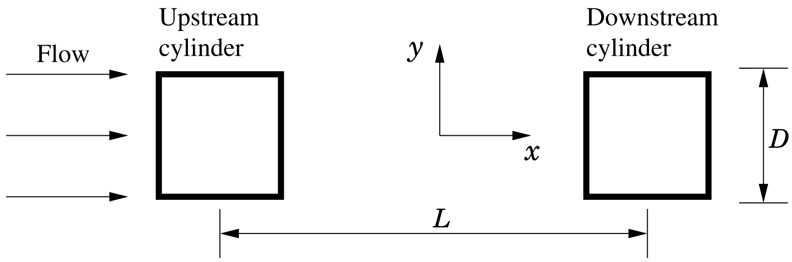

Figure 9. Square cylinders in tandem configuration.

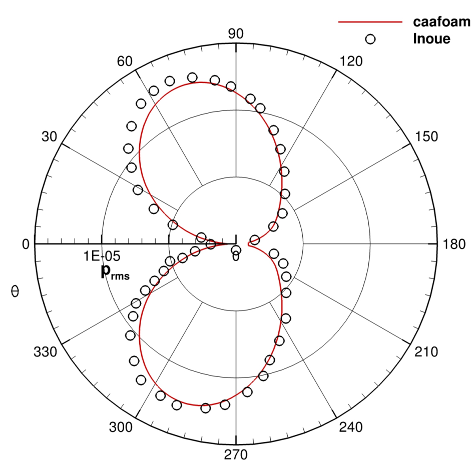

(a) Solver validation, $r/D = 75$

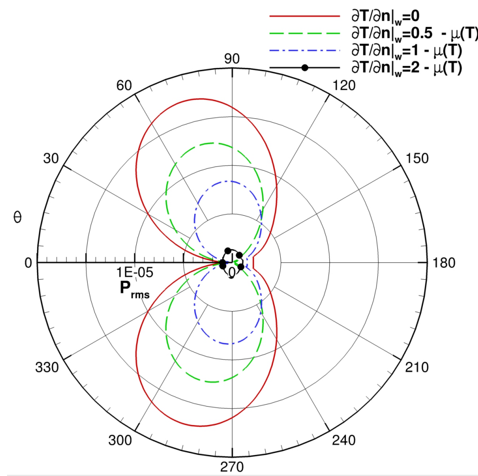

(b) Wall heating effect

Figure 10. Square cylinders in tandem configuration. Acoustic pressure results.

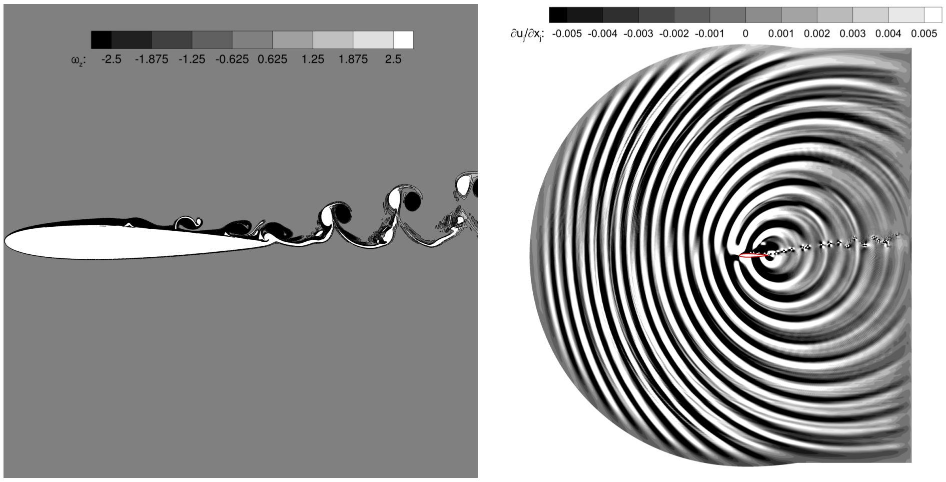

(a) Spanwise vortcity (b) Dilatation rate

Figure 11. Flow and acoustic field representation, NACA 0012 airfoil. Grid G4.

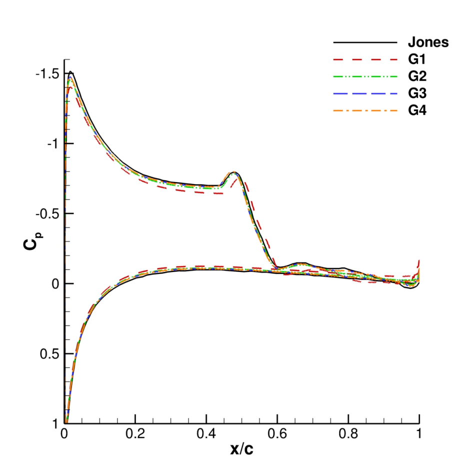

(a) $\overline{c_p}$–x/c

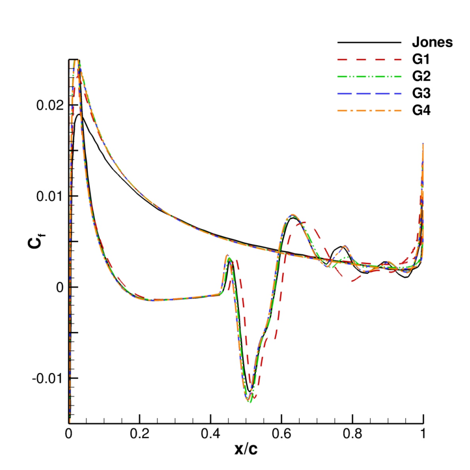

(b) $\overline{c_f}$–x/c

Figure 12. Time-averaged pressure and skin friction coefficient distribution

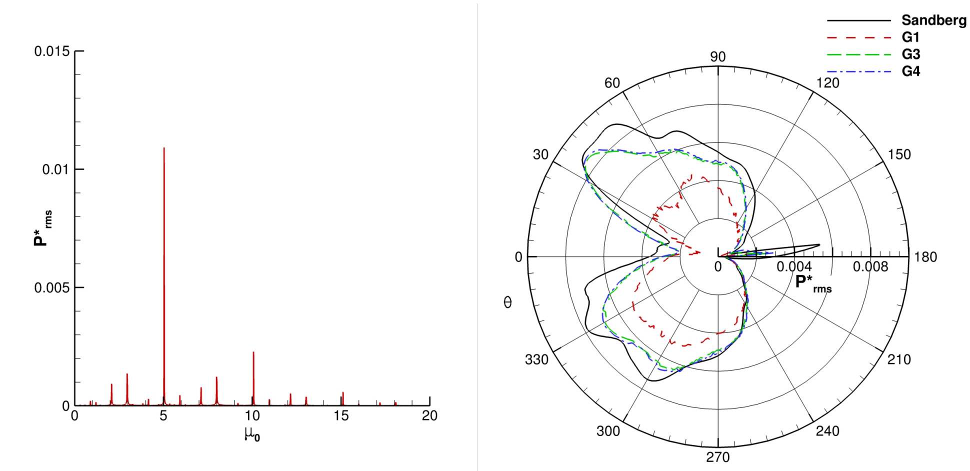

(a) Frequency spectrum, Grid G4.

(b) Polar plot–$\mu_0 = 5.036$

Figure 13. Dimensionless acoustic pressure data. NACA 0012 airfoil.

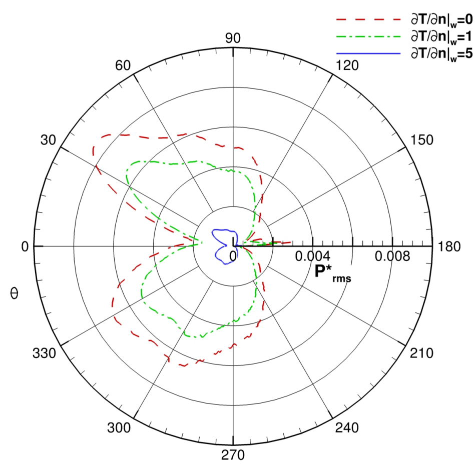

(a) $\mu_0 = 5.036$

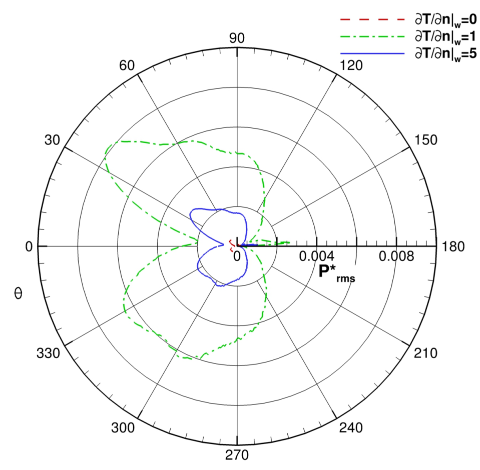

(b) $\mu_0 = 5.044$

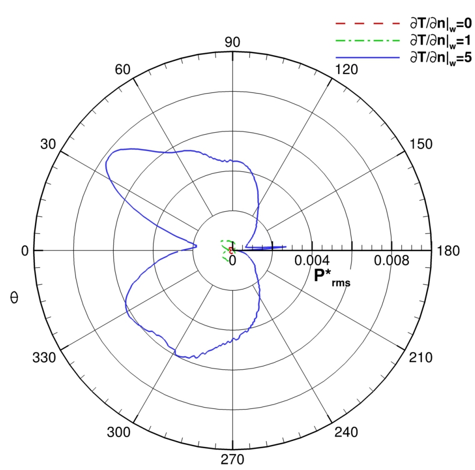

(c) $\mu_0 = 5.061$

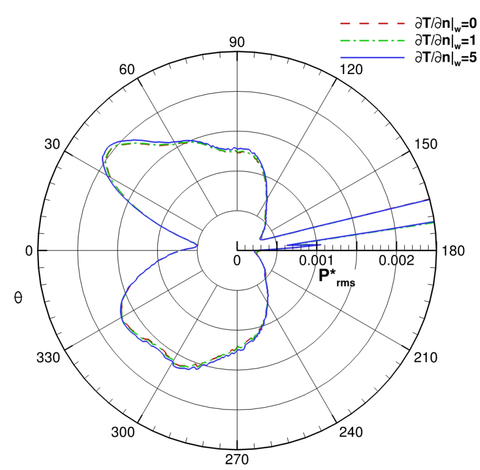

(d) Overall frequencies contribution

Figure 14. Thermal effect on the acoustic pressure, NACA 0012, Grid G4.

Table 1
Circular Cylinder - Re $= 150$, $\mathrm{M}_\infty = 0.2$, $\mu = cost$ - Force coefficients.

Case	ΔC_L	$C_{L,rms}$	$\Delta C_D \cdot 10^2$	$\overline{C_D}$	St
$\partial T/\partial n\|_w = 0$	0.52	0.37	2.56	1.333	0.182
$\partial T/\partial n\|_w = 0.5$	0.49	0.35	2.45	1.333	0.182
$\partial T/\partial n\|_w = 1$	0.46	0.33	2.25	1.327	0.181
$\partial T/\partial n\|_w = 2$	0.41	0.29	1.96	1.323	0.180
$T_w = 2T_\infty$	0.36	0.25	1.61	1.335	0.177
$T_w = 3T_\infty$	0.25	0.18	0.96	1.327	0.170

Table 2
Circular Cylinder - Re $= 150$, $\mathrm{M}_\infty = 0.2$, $\mu = \mu(T)$ - Force coefficients.

Case	ΔC_L	$C_{L,rms}$	$\Delta C_D \cdot 10^2$	$\overline{C_D}$	St
$\partial T/\partial n\|_w = 0$	0.52	0.36	2.56	1.333	0.182
$\partial T/\partial n\|_w = 0.5$	0.47	0.33	2.21	1.329	0.180
$\partial T/\partial n\|_w = 1$	0.41	0.29	1.84	1.325	0.178
$\partial T/\partial n\|_w = 2$	0.31	0.22	1.14	1.315	0.173
$T_w = 2T_\infty$	0.24	0.17	0.67	1.382	0.161
$T_w = 3T_\infty$	0.08	0.06	0.07	1.402	0.139

Table 3
Square Cylinder Side by Side, $L/D = 3,$ in phase - $\mathrm{Re} = 150,\ \mathrm{M}_\infty = 0.2,\ \mu = \mu(T)$ - Force coefficients.

Case	ΔC_L	$\overline{C_L}$	ΔC_D	$\overline{C_D}$	St
$\partial T/\partial n\|_w = 0$	0.41	±0.075	0.114	1.592	0.155
$\partial T/\partial n\|_w = 0.5$	0.39	±0.096	0.101	1.589	0.151
$\partial T/\partial n\|_w = 1$	0.35	±0.119	0.087	1.589	0.149
$\partial T/\partial n\|_w = 2$	0.26	±0.163	0.061	1.591	0.146

Table 4
Square cylinders in tandem configuration, $L/D = 2$, $\mathrm{Re} = 150,\ \mathrm{M}_\infty = 0.2,\ \mu = \mu(T)$ - Force coefficients.

Upstream cylinder

Case	$\Delta C_L \cdot 10^2$	$\overline{C_L} \cdot 10^4$	$\Delta C_D \cdot 10^4$	$\overline{C_D}$	St
$\partial T/\partial n\|_w = 0$	1.951	0	1.05	1.28	0.134
$\partial T/\partial n\|_w = 0.5$	1.118	0.48	0.47	1.27	0.128
$\partial T/\partial n\|_w = 1$	0.631	1.10	0.15	1.26	0.122
$\partial T/\partial n\|_w = 2$	0.043	0.07	2.90	1.20	0.105

Downstream cylinder

Case	$\Delta C_L \cdot 10^2$	$\overline{C_L} \cdot 10^4$	$\Delta C_D \cdot 10^4$	$\overline{C_D}$	St
$\partial T/\partial n\|_w = 0$	5.30	0	7.65	-0.196	0.134
$\partial T/\partial n\|_w = 0.5$	3.80	2.42	3.21	-0.158	0.128
$\partial T/\partial n\|_w = 1$	2.59	3.79	1.16	-0.114	0.122
$\partial T/\partial n\|_w = 2$	0.26	7.40	0.87	-0.010	0.105

Table 5
Computational domain discretisation.

Grid	N_{foil}	N_{radial}	N_{wake}	N_{tot}
G1	1084	690	755	1789860
G2	2000	690	755	2421900
G3	4000	690	755	3801900
G4	4000	800	1000	4800000

Table 6
Time-averaged lift and drag coefficients.

	G1	G2	G3	G4	Jones [28]
$\overline{C_L}$	0.439	0.473	0.484	0.484	0.499
$\overline{C_D} \cdot 10^2$	3.13	3.16	3.17	3.17	3.07

Table 7
NACA 0012, $\mathrm{Re} = 5 \cdot 10^4$, $\mathrm{M}_\infty = 0.4$. Wall heating impact

	$\partial T/\partial n\|_w = 0$	$\partial T/\partial n\|_w = 1$	$\partial T/\partial n\|_w = 5$
$\overline{C_L}$	0.484	0.484	0.484
$\overline{C_D} \cdot 10^2$	3.17	3.17	3.20
$C_{L_{RMS}} \cdot 10^2$	1.87	1.88	1.91
$C_{D_{RMS}} \cdot 10^3$	2.02	2.05	2.16
μ_0	5.036	5.044	5.061